Supplementary material for：

The micro electroforming of precision mold inserts with high flatness via internal stress reduction and interfacial bonding enhancement

ZHANG Lu(张露)[1, 2], LI Meng-yao(李孟垚)[1, 2], LUO Xue-bao(罗雪宝)[3],
YANG Di(杨迪)[1,2], LIU Bo(刘波)[1, 2] , HUANG Jing(黄晶)[4],
MA Zhi-gao(马志高)[1, 2]*, LI Zhou(李洲)[1, 2]*

1. State Key Laboratory of High Performance Complex Manufacturing (Central South University), Changsha 410083, China;
2. College of Mechanical and Electrical Engineering, Central South University, Changsha 410083, China;
3. Xi'an Space Engine Company Limited, Xi'an 710100, China;
4. The First Affiliated Hospital of Shaoyang University, Shaoyang 422001, China

© Central South University 2026

The supplementary materials consist of 7 pages in total, including 6 figures, 3 tables, and 14 references.

Part 1: Simulation procedure based on the equivalent reference temperature method

The simulation of internal stress in the Ni electrodeposited layer was conducted using the thermal expansion subnode within the solid mechanics module of COMSOL. Based on the main steps of the finite element method, the simulation procedure was as follows:

(1) Geometric model construction: a geometric model of the Ni electrodeposited layer and stainless-steel substrate was established based on the actual electroforming process conditions, as shown in Figure S1. The stainless-steel substrate had dimensions of 30 mm × 30 mm × 1 mm, while the nickel layer measured 25 mm × 25 mm × 0.06 mm. Both materials were assumed to be isotropic and homogeneous. The physical properties were obtained from the materials database, as listed in Table S1.

(2) Mesh generation: the thickness of the electrodeposited layer was 60 μm, and the stainless-steel substrate was 1 mm thick. Due to the significant difference in thickness between the two layers and the tendency for warpage to occur at the edges of the electrodeposited layer, a combination of sweep and mapped meshing was adopted. This method improved the computational accuracy at the interface between the electrodeposited layer and the substrate, as well as at the edges of the electrodeposited layer, as shown in Figure S 2.

(3) Application of constraints and loads: To reflect the actual electroforming conditions, fixed constraints were applied to the bottom surface and all four side surfaces of the stainless-steel substrate. The actual electroforming process temperature T_p was set to 323.15 K. Based on equations (S-1) and (S-2), the range of the equivalent reference temperature T_{ref} was determined. Then, a thermal load was applied to the Ni electrodeposited layer. Since the experimentally measured internal stress in the Ni was tensile, the thermal expansion behavior was modeled accordingly. The equivalent reference temperature T_{ref} was higher than the actual electroforming temperature T_p. A virtual cooling process from T_{ref} to T_p was used to apply the thermal load, during which the temperature of the stainless-steel substrate remained unchanged. The experimentally

measured internal stress σ_0 and the thermal load ΔT in the simulation satisfy the following relationship:

$$\Delta T = -\frac{1-v}{E} \times \frac{\sigma_{re}}{\alpha} \tag{S-1}$$

$$\Delta T = T_p - T_{ref} \tag{S-2}$$

The equivalent reference temperature T_{ref}, until the error δ between the simulated internal stress σ_c and the experimentally determined stress σ_0 was less than 1%. The corresponding T_{ref} was then defined as the equivalent reference temperature for the simulation model.

$$\delta = \frac{|\sigma_c - \sigma_0|}{|\sigma_0|} \leq 1\% \tag{S-3}$$

(4) Simulation Calculation: a thermal load was applied to analyze the warpage deformation of the Ni electrodeposited layer at different electrodeposition thicknesses. Based on the determined equivalent reference temperature T_{ref}, thermal loads were applied to nickel electrodeposited layers of different thicknesses to obtain the corresponding warpage deformation.

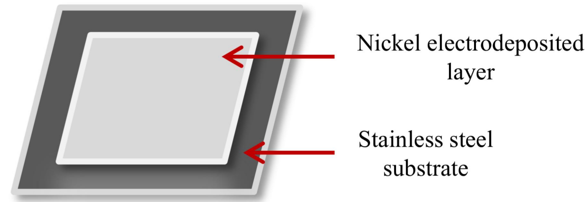

Figure S1 Geometric model for the warpage deformation simulation of the electrodeposited layer

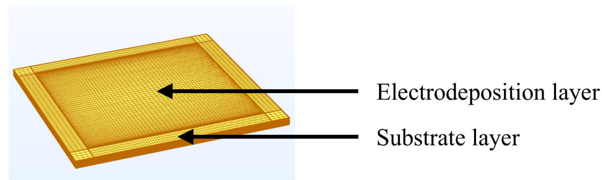

Figure S2 The meshed geometric model used in the simulation study of electrodeposition layer internal stress

Table S1 Physical properties of materials used in the simulation model

Material	Elastic modulus/MPa	Poisson's ratio	Coefficient of thermal expansion/°C
Nickel	2.07E+5	0.30	1.33E-5
304 stainless steel	1.93E+5	0.29	1.73E-5

Given that the current density of 1 A/dm^2 results in relatively low internal stress, it leads to smaller warpage deformation during the electrodeposition process. Therefore, the base layer was deposited at a current density of 1 A/dm^2. The internal stress in the electrodeposited layer was equivalently modeled by applying different thermal loads [1]. When the equivalent reference temperature T_{ref} set to 362.15 K, the simulated internal stress σ_c as 136.78 MPa, with an error of less than 1% compared to the internal stress measured by XRD. Finally, the equivalent reference temperature was determined to be 362.15 K, and the stress distribution in the Ni electrodeposited layer at this temperature is shown in Figure S 3. The same thermal load was applied to Ni electrodeposited layer with different thicknesses (60, 100, 140, 180, 220, 240, and 260 μm).

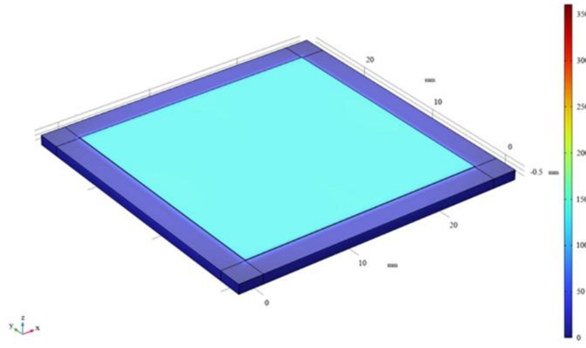

Figure S 3 Stress distribution in the Ni electrodeposited layer at the equivalent reference temperature of 362.15 K

Part 2: XRD stress measurement principle and hydrogen evolution current efficiency calculation method

Internal stress measurement via XRD relies on the principle that internal stress within a material induces changes in the interplanar spacing, which in turn affects the diffraction angle and the position of diffraction peaks generated when X-rays irradiate the crystal surface [2–4]. According to Bragg's law, the stress σ_ϕ on the sample surface (lying within the diffraction plane) can be calculated by measuring the shift in diffraction peak positions along at least two directions defined by the angle ψ. The relevant formulas are presented below:

$$n\lambda = 2d\sin\theta \tag{S-4}$$

$$\sigma_\phi = -\frac{E}{2(1+v)}\cot\theta_0 \frac{\pi}{180}\frac{\partial(2\theta)}{\partial(\sin^2\psi)} \tag{S-5}$$

Where E, v, θ_0, and θ represent the Young's modulus, Poisson's ratio, diffraction angle without stress, and diffraction angle under stress of the test sample, respectively.

The hydrogen evolution current efficiency is given by:

$$\eta_{H_2} = \left(1 - \frac{2mF}{ItM_{Ni}}\right)\times 100\% \tag{S-6}$$

Where η_{H_2} represents the hydrogen evolution current efficiency, m represents the mass (g) of electrodeposited nickel, F represents the Faraday constant (96485 C/mol), I represents the current (A), t represents the time (s), and M_{Ni} represents the molecular weight of nickel (58.69 g/mol).

Part 3: Sample preparation and measurement results for metal layer thickness

To facilitate film thickness measurement, the silicon wafer was partially covered with adhesive tape prior to magnetron sputtering, and the entire sample was then placed in a magnetron sputtering system for deposition. After sputtering, the adhesive tape was peeled off, creating a height difference between the tape-covered and uncovered areas of the wafer. The thicknesses of various sputtered films, including multiple interlayers and a conductive layer, are shown in Figure S4. The corresponding specific values are listed in Table S2.

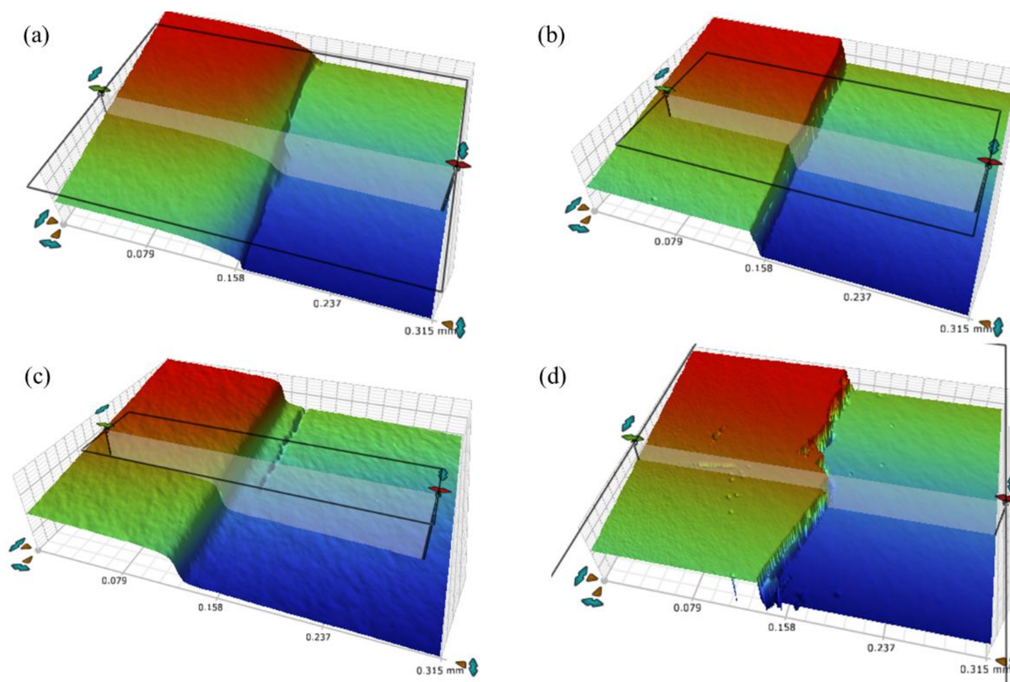

Figure S 4 The 3D profile of different target thickness measurements: (a) Pt; (b) Cr; (c) Ni; (d) Ti

Table S2 Results of thickness measurements and sputtering rate

Target materials	Thickness 1 /nm	Thickness 2 /nm	Thickness 3 /nm	Average thickness /nm	Time /s	Rate /($nm \cdot s^{-1}$)
Pt	274	271	273	273	900	0.303
Cr	261	263	259	261	600	0.435
Ni	154	152	150	152	800	0.190
Ti	248	246	248	247	800	0.275

Part 4: Low-magnification SEM analysis

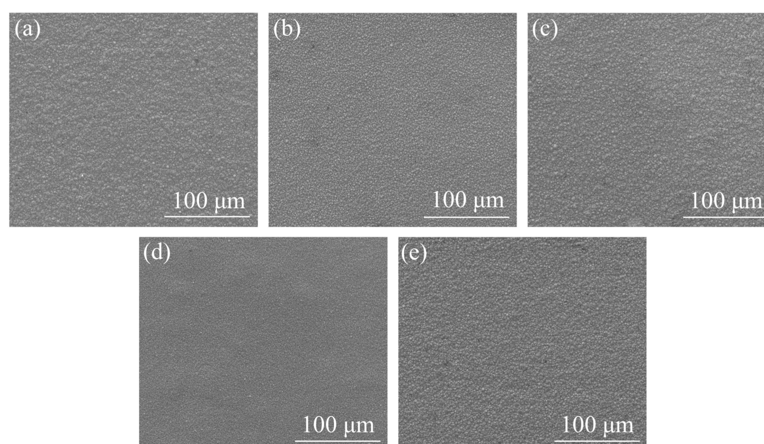

Figure S5 SEM images of Ni electrodeposits at different pH: (a) 3.50; (b) 3.75; (c) 4.00; (d) 4.25; (e) 4.50

Observation results indicated that varying bath pH values did not significantly alter the surface morphology, with no observable protrusions or pore structures (Figure S 5). However, minimal porosity was detected on the layer deposited at pH 3.75, suggesting relatively intense hydrogen evolution reaction at this condition. Similarly, distinct protrusions or pore defects were absent across different electroforming

temperatures (Figure S 6). Yet pinholes emerged on sample fabricated at 60 °C, implying enhanced hydrogen evolution with elevated temperature. Crucially, hydrogen evolution negligibly affected overall surface morphology, and its intensity remained largely temperature-insensitive within the studied range.

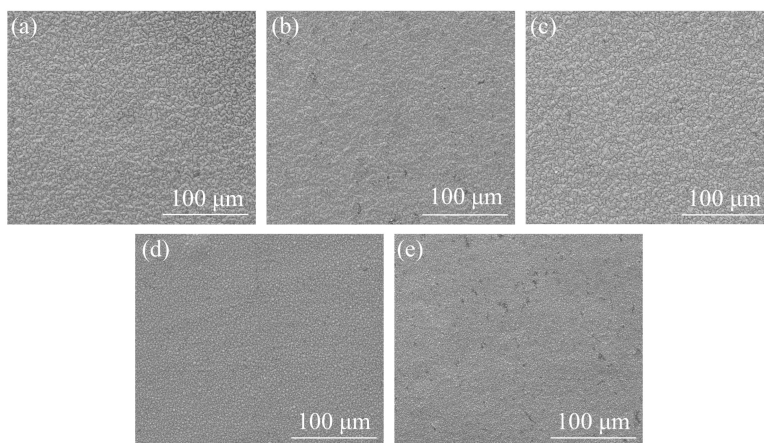

Figure S 6 SEM images of Ni electrodeposits at different temperatures: (a) 20 °C; (b) 30 °C; (c) 40 °C; (d) 50 °C; (e) 60 °C

Part 5: XRD pattern and dislocation density analysis method

To quantify the crystal growth orientation of the electroformed nickel layer, the relative texture coefficient (RTC) was derived from the XRD patterns using the following equation [5,6]:

$$RTC = \frac{I_{(hkl)} / I^{0}_{(hkl)}}{\sum_{i=1}^{n} I_{(hkl)} / I^{0}_{(hkl)}} \times 100\% \tag{S-7}$$

Where $I_{(hkl)}$ denotes the integrated diffraction intensity of the (hkl) crystallographic plane, $I^{0}_{(hkl)}$ represents the corresponding intensity from the nickel standard powder diffraction card. The term $\sum_{i=1}^{n} I_{(hkl)}/I^{0}_{(hkl)}$ corresponds to the sum of intensity ratios for the (111), (200), and (220) diffraction peaks relative to their standard reference values.

To accurately assess diffraction peak broadening caused by grain refinement and lattice distortion, the Voigt function was employed for spectral line fitting [7,8]. After obtaining integral broadening quantities β_C grain refinement) and β_G micro strain), crystallite size and micro strain were calculated using the Scherrer formula and micro strain definition as follows [9] :

$$D = \frac{k\lambda}{\beta_C \cos\theta} \tag{S-8}$$

$$\varepsilon = \frac{\beta_G}{4\tan\theta} \tag{S-9}$$

Where D denotes grain size (nm), and ε is the micro strain, k represents a dimensionless constant typically valued at 0.9, λ corresponds to the X-ray wavelength (1.5406 Å for Cu Kα radiation), while β and θ designate the full width at half maximum and diffraction angle, respectively.

According to Wagner's chaotic dislocation distribution model [10,11], dislocations in crystal sub-boundaries and micro strain within sub-blocks are characterized by a unified dislocation density, enabling calculation of the average dislocation density ρ through the following expression:

$$\rho = \frac{3\sqrt{2\pi}\varepsilon}{1.25D\bar{b}} \tag{S-10}$$

Where $\bar{b}$ is the Bergstrom vector (0.249 nm), and other symbols retain their previously defined meanings.

Part 6: The density and mechanical properties of each layer

Pt was chosen as the conductive layer in the study due to its good electrical conductivity combined with a relatively high yield strength. As for the interlayer, Ti was selected because of its high yield strength and low elastic modulus. This combination allows Ti to absorb energy through deformation under applied stress, thereby helping to maintain structural integrity and prevent failure. Consequently, Ti emerged as the preferred interlayer material in scratch tests.

The properties of thin films differ from those of bulk materials, and material characteristics can vary across different systems. This is reflected in Table S3, where the yield strength of Ti is presented as the average of three different samples from the literature [12]. Therefore, the conclusions and data provided here are for reference.

Table S3 The physical properties of each conductive metal layer [12–14]

Material	Density /(g·cm³)	Yield strength /MPa	Young's modulus /GPa	Electrical resistivity /(Ω·μm)
Pt	21.090	180	168	0.1050
Cr	7.190	140	279	0.1250
Ni	8.908	138	200	0.0693
Ti	4.507	196	116	0.4200

References

[1] Song C, Du L, Li X, et al. Residual stress modeling and analysis for micro electroforming layer[J]. Microsystem Technologies, 2017, 23(10): 4709-4716.

[2] Li X, Liu J, Wu H, et al. Research progress of residual stress measurement methods[J]. Heliyon, 2024, 10(7): e28348.

[3] Wang D, Yan B, Dang Z, et al. Analysis and mechanism study of residual stress during the spontaneous crystallisation process of molten titanium-containing blast furnace slag[J]. Crystals, 2024, 14(1): 70.

[4] Shao Z, Zhang C, Li Y, et al. A review of non-destructive evaluation (NDE) techniques for residual stress profiling of metallic components in aircraft engines[J]. Aerospace, 2022, 9(10): 534.

[5] Jiang B, Ma Z, Yang D, et al. Physical insights into the effects of current parameters on internal stress of Ni electrodeposits[J]. The Journal of Physical Chemistry Letters, 2025, 16(41): 10824-10832.

[6] Zhang L, Yang D, Ma Z, et al. Pulse current electroforming of Ni-PTFE nanocomposite mold insert with long-lifetime and anti-adhesive properties[J]. Electrochimica Acta, 2024, 491: 144308.

[7] Bhagath Singh G V P, Subramaniam K V L. Quantitative XRD Analysis of Binary Blends of Siliceous Fly Ash and Hydrated Cement[J]. Journal of Materials in Civil Engineering, 2016, 28(8): 04016042.

[8] Shixing T, Jing Z, Jing N, et al. In-situ energy calibration of SSRF macromolecular crystallography beamline using powder diffraction[J]. Nuclear Science and Techniques, 2010, 21(6): 321-324.

[9] Sen S K, Barman U C, Manir M S, et al. X-ray peak profile analysis of pure and Dy-doped α -MoO_3 nanobelts using Debye-Scherrer, Williamson-Hall and Halder-Wagner methods[J]. Advances in Natural Sciences: Nanoscience and Nanotechnology, 2020, 11(2): 025004.

[10] Qiang J, Jiang B, Dong Y, et al. Tuning residual stress in electrodeposited nickel films via pulse current[J]. Surfaces and Interfaces, 2023, 40: 103038.
[11] Song C, Du L, Ji X. Reducing the residual stress in micro electroforming layer by megasonic agitation[J]. Ultrasonics Sonochemistry, 2018, 49: 233-240.
[12] Li D, Fan G, Huang X, et al. Enhanced strength in pure Ti via design of alternating coarse- and fine-grain layers[J]. Acta Materialia, 2021, 206: 116627.
[13] Bhattacharyya P. Technological journey towards reliable microheater development for MEMS gas sensors: A review[J]. IEEE Transactions on Device and Materials Reliability, 2014, 14(2): 589-599.
[14] Neubronner M, Bodmer T, Hübner C, et al. D6 properties of solids and solid materials[M]//VDI E. V. VDI Heat Atlas. Berlin, Heidelberg: Springer Berlin Heidelberg, 2010: 551-614.